

1 **Southern Ocean low cloud and precipitation phase observed during the**
2 **Macquarie Island Cloud and Radiation Experiment (MICRE)**

3 Emily Tansey¹, Roger Marchand¹, Simon P. Alexander^{2,3}, Andrew R. Klekociuk^{2,3}, and Alain
4 Protat^{2,4}
5

6 ¹University of Washington, Seattle, Washington, United States

7 ²Australian Antarctic Division, Hobart, TAS, Australia

8 ³Australian Antarctic Partnership Program, Institute for Marine and Antarctic Studies, University of Tasmania,
9 Hobart, TAS, Australia

10 ⁴Australian Bureau of Meteorology, Melbourne, Victoria, Australia
11

12 Corresponding author: Emily Tansey (etansey@uw.edu)

13 **Key Points:**

- 14 • Ground observations at Macquarie Island indicate that low clouds occur ~65% of the
15 time; the majority have cloud top temperatures below 0°C.
- 16 • ~85% of low clouds with top temperatures < 0°C have liquid-phase bases and form
17 precipitation, much of which does not reach the surface.
- 18 • Liquid-phase precipitation directly below cloud base had radar reflectivities < -10 dBZ;
19 reflectivities above 0 dBZ were predominantly ice.

20 Abstract

21 Shallow cloud decks residing in or near the boundary layer cover a large fraction of the Southern
22 Ocean (SO) and play a major role in determining the amount of shortwave radiation reflected
23 back to space from this region. In this article, we examine the macrophysical characteristics and
24 thermodynamic phase of low clouds (tops < 3 km) and precipitation using ground-based
25 ceilometer, depolarization lidar and vertically-pointing W-band radar measurements collected
26 during the Macquarie Island Cloud and Radiation Experiment (MICRE) from April 2016-March
27 2017. During MICRE, low clouds occurred ~65% of the time on average (slightly more often in
28 austral winter than summer). About 2/3 of low clouds were cold-topped (temperatures < 0°C);
29 these were thicker and had higher bases on average than warm-topped clouds. 83-88% of cold-
30 topped low clouds were liquid phase at cloud base (depending on the season). The majority of
31 low clouds had precipitation in the vertical range 150 to 250 meters below cloud base, a
32 significant fraction of which did not reach the surface. Phase characterization is limited to the
33 period between April 2016 and November 2016. Small-particle (low-radar-reflectivity)
34 precipitation (which dominates precipitation occurrence) was mostly liquid below-cloud, while
35 large-particle precipitation (which dominates total accumulation) was predominantly
36 mixed/ambiguous or ice phase. Approximately 40% of cold-topped clouds had mixed/ambiguous
37 or ice phase precipitation below (with predominantly liquid phase cloud droplets at cloud base).
38 Below-cloud precipitation with radar reflectivity factors below about -10 dBZ were
39 predominantly liquid, while reflectivity factors above about 0 dBZ were predominantly ice.

40 Plain Language Summary

41 The Southern Ocean is covered by low altitude cloud decks the majority of the time. Properties
42 like cloud occurrence frequency, particle phase and precipitation habits determine how much
43 solar radiation clouds reflect and how much infrared radiation they emit, which in turn affects the
44 balance of the planet's incoming and outgoing radiation. In this paper, we examine low cloud
45 properties observed from the ground at Macquarie Island, including how frequently they occur
46 and at what temperatures. We study particle thermodynamic phase (liquid, ice or mixed) at cloud
47 base and in precipitation below-cloud. A majority of low clouds are predominantly composed of
48 liquid phase droplets, although frozen precipitation is frequently found below cloud base. Low
49 clouds form precipitation more often than not, much of which evaporates before reaching the
50 ground. In below-freezing low clouds, the majority of large raindrops & snowflakes that do reach

51 the ground originate as frozen precipitation directly below cloud base. This indicates that ice
52 formation is frequently active in clouds composed predominantly of liquid-phase droplets.
53 Lastly, we build upon an established radar-lidar relationship that particles with radar reflectivity
54 factors below -10 dBZ are generally liquid, whereas above 0 dBZ are most often ice phase.

55 1. Introduction

56 Shallow cloud decks residing in or near the boundary layer cover a large fraction of the Southern
57 Ocean (SO) and play a major role in determining the amount of shortwave radiation reflected
58 back to space from this region [Mace 2010, Bodas-Salcedo et al. 2016, Huang et al. 2016]. For
59 many years now, models have struggled to simulate correctly top-of-atmosphere radiative fluxes
60 and the surface energy budget of the SO [Trenberth & Fasullo 2010, Bodas-Salcedo et al. 2016,
61 Schneider & Reusch 2016]. These radiative errors influence local and global atmospheric and
62 oceanic circulations [Ceppi et al. 2012, 2013, Hwang & Frierson 2013, Sallée et al. 2013, Kay et
63 al. 2016] and global climate sensitivity [Gettelman et al. 2019, Bodas-Salcedo et al. 2019,
64 Zelinka et al. 2020]. The radiative bias is smaller on average in the current generation of climate
65 models than in the previous generation (specifically, those participating in the Cloud Model
66 Intercomparison Project phase 6 (CMIP6) relative to phase 5 (CMIP5)), but significant radiative
67 bias remains [Schuddeboom & McDonald 2021, Cesana et al. 2022, Lauer et al. 2023, Mallet et
68 al. 2023].

69
70 Satellite observations indicate that SO stratocumulus clouds (StCu) are predominantly composed
71 of supercooled liquid, at least at cloud top [Huang et al. 2016, Mace et al. 2020, 2021a], and at
72 least for CMIP5 models, several studies found that the radiative bias was related to the incorrect
73 partitioning of the cloud phase (ice vs. liquid) in these shallow clouds, especially in cyclone cold
74 sectors [Bodas-Salcedo et al. 2016, Kay et al. 2016, Frey & Kay, 2017]. While it remains to be
75 seen to what degree phase partitioning is a dominant source of the remaining model radiative
76 bias, it is clear that climate models need to capture well the temperature dependence of clouds
77 (that is, cloud feedbacks) in this region. Zelinka et al. [2020], for example, found in a multi-
78 climate-model analysis that low cloud feedbacks over the SO increased from weakly negative on
79 average in CMIP5 to positive in CMIP6, yielding an overall global cloud feedback which is
80 significantly more positive in CMIP6 (and consequently CMIP6 models have a larger climate

81 sensitivity and greater warming on average). The low cloud feedback increased in CMIP6
82 because models contain more low-altitude liquid clouds and fewer ice clouds. This sensitivity of
83 the cloud feedback to phase arises in models because liquid cloud cover and cloud albedo tend to
84 reduce with warming (a positive cloud feedback), while ice clouds tend to melt to form brighter
85 liquid clouds (a negative cloud feedback). There is reasonable observational support for this
86 overall tendency [e.g., Terai et al 2019]. Nonetheless, low cloud macrophysical properties (such
87 as cloud occurrence and thickness) as well as microphysical properties (such as liquid water
88 content, effective radius and droplet number concentration) that ultimately control the cloud
89 albedo are influenced by many factors including precipitation [Wood 2012].

90
91 Precipitation is very common in SO clouds [Wang et al. 2015, Tansey et al. 2022]. In liquid
92 phase clouds, precipitation is associated with an increase in the effective radius and decrease in
93 cloud liquid water path, both of which lower albedo [Ceppi et al. 2015]. In mixed phase clouds,
94 the presence of ice phase particles substantially impacts the cloud microphysics because ice
95 particles more readily uptake water vapor than liquid particles, growing into precipitation sized
96 particles at the expense of water droplets (the Wegener–Bergeron–Findeisen process) [e.g. Fan et
97 al. 2011]. Ice particles also grow efficiently by accreting liquid cloud droplets, creating rimed
98 particles [Wood 2012]. Precipitation also removes aerosols (dusts and other particulate matter
99 that can serve as cloud-condensation nuclei on which cloud droplets form) from the atmosphere,
100 lowering the cloud droplet concentration [Wood 2012, McCoy et al. 2020]. In particular, Kang
101 et al. [2022] have recently shown that coalescence of liquid cloud droplets (which initiates
102 precipitation) is the primary process through which aerosols are removed from the boundary
103 layer and plays an important (if not dominant) role in controlling droplet concentration in both
104 liquid and mixed phase SO StCu. And of course, all of these microphysical changes can affect
105 cloud lifetime and thereby the time-average cloud cover.

106
107 But how often are SO low clouds producing frozen or mix-phase precipitation? Based on ship
108 data, Mace and Protat [2018] (hereafter MP18) show ice phase precipitation falls from SO StCu
109 more often than spaceborne lidar suggest. Based on depolarization lidar observations from the
110 ship-based Clouds, Aerosols, Precipitation, Radiation and Atmospheric Composition over the SO
111 (CAPRICORN I) experiment in March and April 2016, MP18 found that between 20% and 40%

112 of cold-topped ($< 0^{\circ}\text{C}$) SO StCu cloud layers were found to have ice or mixed-phase
113 precipitation falling from their cloud base, while at the same time appearing to be
114 overwhelmingly liquid phase (at cloud top) based on depolarization measurement by the Cloud-
115 Aerosol Lidar and Infrared Pathfinder Satellite Observation (CALIPSO). MP18 (as well as a
116 more detailed study by Mace [2020]) conclude that because visible photons are largely absorbed
117 or backscattered within a few optical depths of cloud top, CALIPSO does not identify the
118 presence of ice in the SO StCu because ice often exists deeper within the cloud. Consequently,
119 measurements from the surface are essential to our understanding of cloud-base and below-cloud
120 precipitation phase.

121
122 Few surface-based observational datasets exist across the SO that can be used to assess cloud and
123 precipitation phase. One such dataset is the surface-based observational record from the
124 Macquarie Island Cloud and Radiation Experiment (MICRE), which took place between March
125 2016 and March 2018 [Mcfarquhar et al. 2021]. Macquarie Island (54.5°S , 158.9°E) has a
126 narrow isthmus at its northernmost tip where surface meteorology and tipping bucket rainfall
127 data have been recorded by the Australian Bureau of Meteorology (BoM) since 1948. The station
128 is situated in the middle of the SO storm track and is therefore a suitable location to observe SO
129 cloud and precipitation systems carried by prevailing westerly winds. During MICRE, the U.S.
130 Department of Energy Atmospheric Radiation Measurement (ARM) program, Australian
131 Antarctic Division (AAD) and BoM collaboratively deployed ground instrumentation with the
132 goal of measuring cloud, precipitation, and radiative characteristics. To date, MICRE surface
133 radiation and surface precipitation properties have been analyzed in detail by Hinkelman &
134 Marchand [2020] and Tansey et al. [2022], respectively. In this article we focus on cloud base
135 and below-cloud precipitation phase, relying on the Vaisala CTK-25 ceilometer (905 nm;
136 supplied by ARM), W-band cloud radar (supplied by BoM), and AAD polarization lidar (532
137 nm). Two Vaisala ceilometers were operating during MICRE, one deployed by ARM and one by
138 the University of Canterbury. The instruments were concurrently available for the period of
139 April-November 2016, providing us with some ability to comment on seasonal characteristics.

140
141 Section 2 of this paper outlines the MICRE data, retrievals and sources of uncertainty. Results
142 are presented in section 3, organized in terms of basic cloud macrophysical characteristics at

143 Macquarie Island (section 3.1), cloud base phase (section 3.2), below-cloud precipitation phase
144 (section 3.3), the relationship between radar dBZ and lidar depolarization ratios (section 3.4) and
145 lastly, a comparison of lidar below-cloud properties to the blended surface precipitation data
146 product of Tansey et al. [2022] (section 3.5). A summary and discussion is given in section 4.

147 2. Data and methods

148 Much of the analysis presented in this article is based on the determination of the cloud base
149 phase and the phase of precipitation just below cloud base. Following a brief description of the
150 measurements and the approach used to determine cloud boundaries in Section 2.1 and the lidar
151 calibration in section 2.2, the techniques used to determine cloud-base and precipitation phase
152 are given in section 2.3 and 2.4, respectively.

153 154 2.1 Cloud macrophysical characteristics: ceilometer, W-band radar and radiosondes

155 Basic cloud macrophysical properties (low cloud occurrence, number of low cloud layers, and
156 cloud top and base temperatures) are determined using a combination of radiosonde temperature
157 profiles, along with W-band cloud radar and laser ceilometers. Specifically, cloud base height
158 (CBH) is determined using a Vaisala ceilometer [Münkel et al. 2007, Kuma et al. 2020], and
159 cloud top heights (CTH) from a combination of W-band radar and ceilometer (details follow
160 below). The radar, the Bistatic rAdar SysTem for Atmospheric studies (BASTA) [Delanoë et al.
161 2016], operated in several modes which have been merged to produce a time-height record of
162 radar reflectivity and Doppler velocity on a 12-second-by-25-m time-height grid, with a
163 minimum detectable signal (MDS) of about -40 dBZ at 1 km. The MDS is sufficient to detect
164 essentially all precipitating clouds near the surface, but the radar does at times miss non-
165 precipitating clouds that are detected by the ceilometer. Details on the radar calibration can be
166 found in Tansey et al. [2022], and a complete listing of all the cloud and precipitation
167 instruments deployed during MICRE can be found in McFarquhar et al. [2021].

168
169 The determination of cloud and precipitation boundaries begins by finding contiguous vertical
170 regions (hereafter layers) of significant reflectivity (greater than the MDS) for each 12-second
171 radar profile, with at least 100 m of clear sky (no significant reflectivity) between the layers.
172 The ceilometer vendor's proprietary software appears to assign the cloud base at (or near) the

173 peak in the measured backscatter, which in many cases will be slightly above the location where
174 small cloud droplets can be found, i.e. the cloud base height (CBH). The ceilometer identifies
175 CBH for up to 3 cloud layers (about once every 6 to 15 seconds, depending on the ceilometer).
176 The ceilometer CBHs (regardless of which ceilometer observed it) are mapped onto the 12-
177 second radar grid by aggregating all ceilometer CBHs within 30 seconds of each radar profile
178 and assigning each CBH to the nearest radar layer, as long as the ceilometer CBH is no further
179 than 100 m from the radar layer. (This 100 m allows for errors in the height determination, and
180 for cases where the radar may be able to detect cloud top but not the less reflective region near
181 cloud base). The result is a set of layers, each defined by a radar base height, a radar cloud top
182 height, and a ceilometer cloud base height (taken as the median value of all the CBHs assigned to
183 the layer). As will be discussed later, precipitation falling from low clouds is common place, and
184 the radar layer base height is typically lower than the ceilometer CBH. Ceilometer CBHs which
185 are more than 100 m from a known (radar) layer are taken to be part of an additional layer whose
186 reflectivity is below the radar MDS, and its position is defined only by the median ceilometer
187 CBH. This occurs about 10% of the time.

188

189 For the presented analysis, the above 12-second boundaries are further reduced onto a 5-minute
190 grid, as described in this paragraph. A 5-minute grid is needed in part to obtain sufficient laser
191 backscatter signal to estimate cloud base phase and the below-cloud precipitation phase; but this
192 grid also substantially reduces the impact of noise in the radar boundaries and surface
193 precipitation datasets. If at least one cloud layer is reported for at least one minute (at least 5 of
194 the 25 12-second columns in each 5-minute period has a ceilometer CBH), we define the 5-
195 minute analysis period as cloudy, and CBH is taken as the median CBH (i.e. the median when
196 present). If the ceilometer reports more than one cloud base is present for at least one minute, we
197 defined the cloud as multi-layered and the 5-minute median CBH is calculated for each layer.
198 We likewise compute 5-minute median CTHs from the radar layer top heights (median when
199 present).

200

201 The associated radiosonde temperature, and all phase retrievals, are based on the 5-minute
202 median CTH & CBH pair from the cloud layer nearest to the surface, and “low clouds”
203 specifically refers to clouds with a 5-minute median CTH < 3 km. As a sensitivity test, we re-

204 calculated the cloud occurrence statistics (presented in section 3.1) but instead of using 1 minute
205 (out of 5 minutes) as minimum requirement to identify cloud, we increased the threshold to 2
206 minutes. This causes the single-layer cloud occurrence frequency to increase by less than 3% at
207 the expense of multi-layer occurrence, and total cloud occurrence did not change significantly
208 (within the listed uncertainties).

209

210 To calculate cloud top temperature (CTT), twice-daily radiosonde launches at 00:00 UTC and
211 12:00 UTC are paired with radar/ceilometer cloud boundaries for the surrounding 12 hours of the
212 launch. Some degree of uncertainty is expected in CTTs far from sonde launch times, as the
213 vertical temperature profile may evolve over the course of the 12 hour period. To test the
214 sensitivity of our results, statistics were re-calculated for the surrounding 6 hours of a launch,
215 effectively halving the sample size. Results were within the estimated uncertainty ranges
216 discussed below. Tightening the time range surrounding sonde launches did decrease the
217 estimated retrieval error rate for cloud base thermodynamic phase (estimated using warm-topped
218 clouds, discussed in the next section), but only by about 1%.

219

220 2.2 Depolarization Lidar

221 In addition to the laser ceilometers, the AAD deployed a 532 nm depolarization lidar. The lidar
222 operated at 30 m vertical resolution, with further specifications given in Klekociuk et al. [2020]
223 and Huang et al. [2015], and provided range-profiles of backscatter and depolarization ratio. We
224 initially attempted to calibrate the AAD lidar following the method of O'Connor [2004], which
225 relies on periods of fully attenuating, non-precipitating cloud. Unfortunately, we found the AAD
226 calibration was not stable across the 7-month measurement period, sometimes changing
227 significantly from one non-precipitating calibration period to the next. However, we found that
228 we could calibrate the ceilometer using the O'Connor [2004] approach and that this calibration
229 was stable over time. Therefore, in order to better calibrate the AAD system data, we developed
230 an approach that scales the AAD polarization lidar backscatter to the stably-calibrated ceilometer
231 backscatter for times that are far from periods where the O'Connor technique can be applied.
232 Further details on this calibration transfer approach can be found in the Supporting Information,
233 where we show that the transfer calibration factors compare well with calibration factors directly

234 from the O’Connor method (during periods where such can be applied directly to the AAD
235 lidar).

236
237 The AAD lidar also malfunctioned for 17 days during August and September, and these data are
238 not included in the analysis. An artificial increase in the cross-polarization channel counts
239 occurred from August-October, which we account for by scaling the depolarization ratios by a
240 correction factor (see Supporting Information section S2). The AAD lidar was also pointed 4° off
241 zenith to vastly reduce (but not quite eliminate) the effects of horizontally oriented ice crystals.
242 The fractional occurrence of missing/bad data are given in section 3.2. We discuss the
243 implications of the lidar data quality concerns in more detail in the concluding section.

244

245 2.3 Below-cloud precipitation

246
247 In Tansey et al. [2022], we give statistics of precipitation measured at the surface by blending
248 data from the radar, disdrometer and tipping bucket for the first year of MICRE (April 2016 –
249 April 2017). In this paper, we examine the thermodynamic phase of hydrometeors which were
250 below-cloud base but evaporated/sublimated before reaching the surface. We specifically use the
251 phrase “below-cloud” to mean the region 150 to 250 m below cloud base. Following MP18,
252 frozen precipitating particles below cloud base polarize the returned backscatter and increase the
253 measured depolarization ratio (δ_L), whereas scattering from spherical liquid drops has a small
254 depolarization ratio. Unlike the situation in-cloud or at cloud base (section 2.4), multiple
255 scattering has a minimal impact on the measured depolarization ratio below-cloud and can be
256 neglected.

257

258 Based on an analysis of warm-topped clouds for which we know the precipitation must be liquid,
259 we find 86% of these data have a $\delta_L \leq 0.05$, and only 7% have a $\delta_L > 0.1$. As we will discuss in
260 section 2.4, seeder-feeder events can result in frozen/mixed phase particles below warm-topped
261 clouds, and may be responsible for δ_L being larger than 0.05, and we have removed such events
262 where we can. Nonetheless, it remains possible that seeding had occurred just prior to the cloud
263 advecting over the radar, and is therefore still affecting the cloud though it is no longer obvious
264 in the radar time-height data. Likewise, surface fog may result in multiple scattering that
265 increases the below-cloud δ_L value and, again, we have removed cases containing surface fog to

266 the degree that we can identify them from the ceilometer. Such events may nonetheless be
267 responsible for some values of δ_L being larger than 0.05 some of the time. On the other hand, for
268 events believed to have mixed or ice-phase precipitation at the surface (i.e. events where the
269 surface disdrometer indicates that snow/mixed phase precipitation is present), the below-cloud δ_L
270 is larger than 0.1 about 74% of the time, between 0.05 and 0.1 for 16% of the time, and less than
271 0.05 only 10% of the time. Accordingly, we ascribe below-cloud precipitation with δ_L less than
272 0.05 as liquid phase, between 0.05 and 0.1 as ambiguous or mixed phase, and greater than 0.1 as
273 frozen. We stress that a depolarization ratio less than 0.05 does not guarantee that all particles are
274 liquid, and some frozen or mixed phase particles may be present (but if so, they are not
275 contributing substantially to the measured lidar backscatter), and vice-versa for depolarization
276 ratios larger than 0.1.

277

278 As with all non-coaxial lidar systems, there is incomplete overlap between the AAD lidar's
279 transmission beam and the field of view of the receiver at low altitudes. For this Macquarie
280 Island campaign, we must restrict the analysis to altitudes of at least 250 m altitude above the
281 surface; that is, phase is retrieved at cloud base and in below-cloud precipitation (100 to 200 m
282 below CBH) restricted to $CBH \geq 450$ m. In later sections, phase occurrence statistics are
283 restricted to cases where the lowest cloud base is greater than 450 m from the surface. We report
284 separately on macrophysical occurrence frequencies that include $CBH < 450$ m (Table #1).

285

286 2.4 Cloud Base Phase

287

288 The cloud base thermodynamic phase is retrieved following the approach described in Hu et al.
289 [2007] and Mace et al. [2020]. As with the below-cloud retrieval, the cloud-base phase retrieval
290 also relies on the lidar depolarization ratio (δ_L), but accounts for multiple scattering using the
291 lidar measured layer-integrated attenuated backscatter (γ). Scattering due to spherical (liquid)
292 particles is distinguished from scattering by horizontally-oriented ice crystals (HOI) based on the
293 tendency of HOI to yield high γ and low δ_L . Similarly, randomly-oriented ice crystals (ROI) are
294 identified based on their tendency to yield high δ_L values and low γ as depicted in Figure 1.
295 Figure 1 shows data from warm clouds with $CTT > 0^\circ\text{C}$. Boundaries initially proposed in Hu et
296 al. [2007] to identify liquid phase particles (based on γ vs. δ_L) are plotted in cyan & green.

297 Points that lie above the cyan line are shown by Hu to be HOI, while points below the green line
298 are ROI. Blue & red lines denote adjusted thresholds developed by Mace et al. [2020] for this
299 same purpose. In this study, we use the thresholds defined by Hu to define HOI & ROI (that is,
300 data points located below the green or above the cyan lines are considered HOI & ROI,
301 respectively), and we consider those points located between the Mace & Hu lines to be mixed
302 phase or ambiguous. Only those points between the red & blue Mace lines are considered likely
303 to be liquid phase. As one expects, Figure 1 shows that the vast majority of the warm-topped
304 clouds have a cloud base phase that is identified as liquid (95%).

305

306 Nominally, the Hu/Mace technique can only be applied when the lidar backscatter is fully
307 attenuated by the cloud layer. Following O'Connor [2004], we define the lidar backscatter as
308 fully attenuated if the backscatter drops by at least a factor of 20 from its in-cloud peak value
309 within 300 m of the in-cloud peak. Otherwise, we define the lidar backscatter as either heavily
310 attenuating if the backscatter drops by a factor 10 within 600 m of the peak, or lightly attenuating
311 (if not fully or heavily attenuating). In the event that the lidar is only lightly attenuated for a 5-
312 minute period, we still apply the retrieval technique limiting the layer to 300 m above cloud base.
313 Most low clouds are found to be fully or heavily attenuating, and statistics on the relative
314 occurrence of the cloud base phases (reported in section 3.2) do not change significantly if we
315 exclude these lightly attenuating layers.

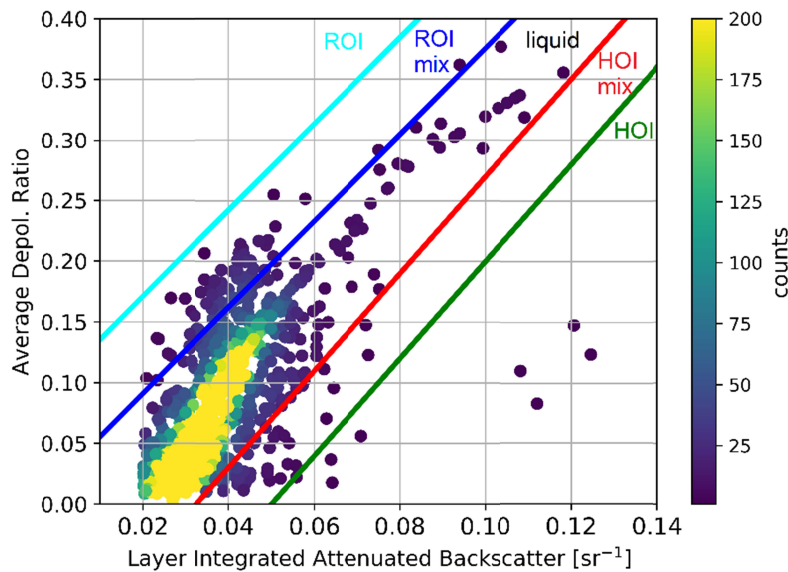
316

317 For the purpose of calculating the integrated backscatter, we define the start of the cloud layer as
318 the region between CBH-100 m (just below the ceilometer defined base) and the first vertical
319 point where the AAD lidar appears to be fully attenuated (no appreciable particulate scattering
320 above this point), or as defined above for heavily and lightly attenuating clouds. We
321 conservatively start at 100 m below ceilometer CBH because the vendor-retrieved cloud base
322 tends to coincide with the peak in total backscatter, which is often somewhat above the altitude
323 where small cloud-droplets can be found (and in which backscatter exponentially increases
324 [O'Connor 2004]). The results do not change appreciably if we increase this level to CBH-50 m.

325

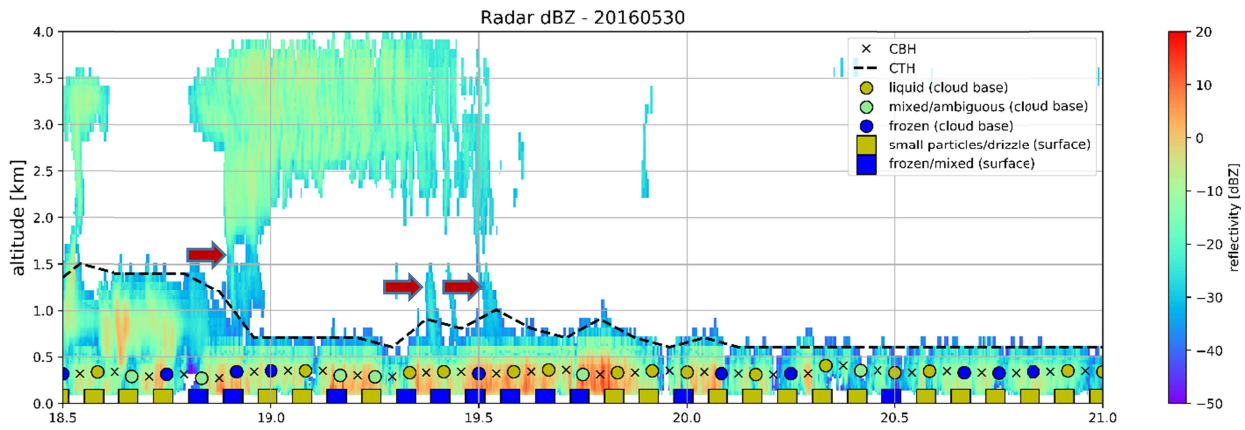
326 Upon visual inspection of individual cases, we found some events where a seeder-feeder
327 mechanism is active in generating ice or mixed phase precipitation from what would otherwise

328 be a warm cloud layer. Figure 2 shows one such case. Here cold clouds aloft are precipitating
 329 glaciated particles into the warm cloud layer near the surface, denoted by the red arrows. The
 330 radar Doppler velocity shows updrafts (negative velocities; purple coloration) near the top of the
 331 higher cloud, which is likely driving ice formation. The large downward Doppler velocity (in
 332 excess of 2.5 m/s), which is associated with the hydrometeors that have fallen from the upper
 333 layer and are now reaching the top of the low cloud (demarcated by the black dashed line),
 334 strongly suggests that the glaciated particles are melting. The nearest sonde puts the freezing
 335 level just above 1700 m. The surface disdrometer data likewise suggest that ice precipitation is
 336 present near the surface during (or around) the times that particles are observed to be falling into
 337 the low cloud. Our simple CTT screening cannot completely account for the presence of seeder-
 338 feeder events because the radar cannot detect all ice falling into the lower layer and can only
 339 show us what is happening when the cloud is above the radar. Where identified, seeder-feeder
 340 cases have been removed from the warm-cloud dataset used to estimate confidence in the phase
 341 retrievals. For the remaining warm-topped cloud cases, only about 5% of the data points in
 342 Figure 1 fall above/below the liquid phase boundaries.

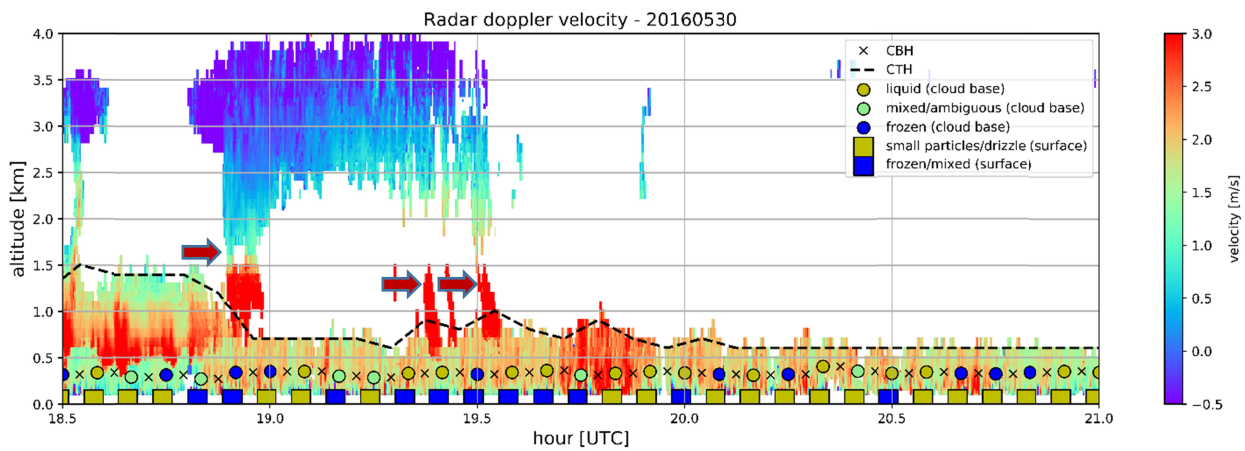


343
 344 *Figure 1: Cloud base layer γ vs. δ_L points for $CTH < 3$ km, $CBH > 450$ m and $CTT > 0^\circ\text{C}$ (i.e. this is for warm/liquid clouds).*
 345 *Lines/categories that identified HOI, ROI and liquid are as defined by Mace et al. [2020]; see text. The colorbar shows density of*
 346 *counts / number of 5-minute observations. Uncertainty is estimated to be about $\pm 2.5\%$ by considering the percentage of points*
 347 *above/below the liquid boundaries (blue and red lines).*

348



349



350

351

352

353

354

Figure 2: Example of a seeder-feeder event in which a higher cloud forms ice particles that seed precipitation in the lower cloud layer. Arrows overlaid on the plot point to obvious seeder-feeder instances. Cloud base height is marked by x's, cloud top height by dashed lines. The phase of particles at cloud base are given by dots (color-coded by phase). Precipitation phase at the surface (squares) are from the MICRE radar-disdrometer blended surface dataset [Tansey et al. 2022].

355

3. Results

356

357

358

359

360

361

362

363

364

365

This section presents results, starting with cloud macrophysical characteristics, specifically seasonal occurrence frequencies of single and multi-layer clouds below 3 km, for cold- and warm-topped clouds. Section 3.2 discusses the occurrence frequencies of various thermodynamic phases at cloud base. Section 3.3 gives occurrence frequencies of precipitation below warm- and cold-topped clouds as well as at the surface. Section 3.3 also examines below-cloud precipitation as a function of cloud base phase. Section 3.4 discusses the relationship between radar dBZ and lidar depolarization ratios in each season (April – November). Lastly, we present below-cloud precipitation depolarization ratios as a function of precipitating particle size (measured at the surface) in section 3.5.

3.1 Basic cloud macrophysics

366
367

368 The MICRE ceilometer, cloud radar and radiosonde datasets span a full annual cycle with only
369 limited data gaps. We provide in Table #1 low cloud occurrence statistics for each season: austral
370 summer (DJF), fall (MAM), winter (JJA) and spring (SON). All percentages are with respect to
371 the number of good samples (that is, the number of 5 minute periods where radar and ceilometer
372 data was collected within 12 hours of a successful sonde launch) in the time period specified.
373 Results in sections 3.2 and 3.3 require polarization lidar, and thus only span April – November
374 2016, and occurrence statistics restricted to this period are also given at the bottom of the Table
375 #1. Uncertainty ranges in all tables are the standard error, calculated as the standard deviation in
376 the daily value divided by the square root of the number of days, treating each day as an
377 independent sample. Estimating the uncertainty in this way provides the uncertainty in the mean
378 for the MICRE period specified, but does not include interannual or other longer term variability.
379 In short, one should not expect that cloud occurrence in another year will necessarily agree with
380 that observed during the MICRE period within the Table #1 uncertainty ranges.

381

382 Percentages in the first two columns are seasonal occurrence frequencies of single and multi-
383 layer clouds with tops below 3 km, respectively. The total of single and multilayer clouds is
384 given in column 3. The data show that low clouds are common in all seasons, with summer
385 (DJF) having only about 10% less cloud cover than winter (JJA). Columns 4 & 5 give the
386 percentage of time that the lowest cloud layer is warm-topped vs. cold-topped. Percentages in
387 columns 4 & 5 sum to the total in column 3. CTT refers to the lowest cloud top in the event that
388 multiple layers are present. The data show that most low clouds had a CTT $< 0^{\circ}\text{C}$. This is true in
389 all seasons, with (not surprisingly) austral winter (JJA) having the highest absolute and relative
390 occurrence of such cold cloud tops. In the annual average, a low cloud layer is present about
391 65% of the time with roughly 2/3 of this cloud having a CTT $< 0^{\circ}\text{C}$.

392

393 The depolarization lidar based phase retrievals (discussed in the next three subsections) is limited
394 to the subset of cases where cloud base is above 450 m. Column 6 gives the percentage of time
395 that cloud top is below 3 km and cloud base is above 450 m, and this is further divided to the
396 occurrence of low clouds with top temperatures $> 0^{\circ}\text{C}$ and $\leq 0^{\circ}\text{C}$ in the final two columns.

407 These three columns are highlighted to emphasize that this is a separate and specific subset of
 408 low clouds used for lidar phase retrievals. The restriction is significant, with the occurrence of
 409 low clouds having a cloud base above 450 m being roughly 20 to 30% lower than the total
 400 occurrence of low clouds, depending on the time period. We will discuss the implications of this
 401 for interpreting the phase statistics in Section 4. Perhaps surprisingly, the difference is roughly
 402 equally split between warm- and cold-topped clouds in all seasons. For example, in winter (JJA)
 403 the occurrence of clouds with $CBH > 450$ m is about 30% lower than the occurrence of all clouds
 404 (that is, 39% of all good data points have low clouds with $CBH > 450$ m, as compared to 69% of
 405 all good data points having a low cloud with any CBH) with 13.6 % of the 30% being due to
 406 warm-topped clouds and the remaining 16.4% being due to cold-topped clouds.

Season	Single layer, CTH<3km, any CBH [%]	Multiple layers with CTH<3km, any CBH [%]	Total CTH<3km, any CBH [%]	CTH<3km, any CBH (lowest layer if multi-layered) and		CTH<3km, CBH>450m (lowest layer if multi-layered) [%]	CTH<3km, CBH>450m and	
				CTT>0°C [%]	CTT≤0°C [%]		CTT>0°C [%]	CTT≤0°C [%]
DJF	50.6±2.1	9.8±1.0	60.4±2.2	22.4±2.4	38.1±2.6	36.8±2.6	7.9±1.3	28.9±2.5
MAM	56.0±2.1	11.1±1.1	67.1±2.1	25.0±2.9	42.0±2.9	39.5±3.0	6.4±1.3	33.1±2.9
JJA	57.9±2.0	11.1±1.0	69.0±2.0	17.8±2.3	51.2±2.7	39.0±2.9	4.2±0.9	34.8±2.9
SON	54.0±2.2	10.2±0.9	64.2±2.4	17.9±2.3	46.3±2.9	44.6±3.1	6.8±1.2	37.8±3.1
MICRE (full year)	54.6±1.0	10.5±0.5	65.1±1.1	20.6±1.2	44.5±1.4	40.4±1.4	6.1±0.6	34.2±1.4
April-Nov.	56.1±1.3	10.5±0.6	66.6±1.3	19.4±1.5	47.2±1.7	40.8±1.8	5.3±0.6	35.5±1.8

407 *Table 1: Low cloud occurrence characteristics. The first two columns show how frequently clouds with radar-lidar-derived tops*
 408 *below 3 km occur in single or multiple layers, respectively, with the total of columns 1 & 2 given in column 3. Columns 4 & 5*
 409 *show warm/cold CTT percentages for the lowest cloud layer. E.g. DJF has single + multi-layer clouds ~60% of the time; warm-*
 410 *topped clouds 22% of the time + cold 38% = 60%. Column 6 shows the occurrence frequency of the subset of clouds used for*
 411 *phase retrievals (tops below 3 km and bases above 450 m). Columns 7 & 8 show warm/cold CTT percentages for the subset of*
 412 *low clouds with $CBH > 450$ m; i.e., $CTT > 0^\circ C + CTT \leq 0^\circ C$ in rows 7 & 8 will sum to the percentage in column 6.*

Season	Warm-topped cloud mean			Cold-topped cloud mean		
	CBH [m]	CTH [m]	Thickness [m]	CBH [m]	CTH [m]	Thickness [m]
DJF	416±22	876±25	460±28	795±41	1674±41	879±56
MAM	360±25	893±40	532±45	737±39	1637±44	900±64
JJA	357±17	826±26	469±29	686±34	1543±41	857±50
SON	376±19	838±21	462±27	822±37	1631±37	809±47
MICRE (full year)	380±10	861±14	481±16	761±19	1620±21	859±27
April-Nov.	356±12	833±18	477±20	749±22	1595±25	847±31

413 *Table 2: Mean boundaries and thicknesses by season for warm-topped ($CTT > 0^\circ C$) and cold-topped ($CTT \leq 0^\circ C$) low clouds*
 414 *($CTH < 3$ km). If multiple layers are present, the lowest cloud layer is used.*

415 Table #2 gives mean cloud boundaries and thicknesses in each season, for the full year of
416 MICRE, and for the April-November period. If multiple layers were present, boundaries for the
417 lowest cloud layer are used in the averaging. Uncertainty in the mean values are again estimated
418 by the standard error (standard deviation divided by the square root of the number of days).
419 Warm clouds occur nearer to the surface (have a lower cloud base and cloud top) and are
420 geometrical thinner on average than cold clouds. The cloud boundaries and thicknesses are
421 fairly similar in all seasons, though arguably the clouds (both warm and cold topped) in winter
422 are a bit closer to the surface than in summer and have lower CBHs and CTHs (with the
423 difference just exceeding the sum of the estimated one-sigma uncertainties).

424

425 3.2 Cloud base phase statistics

426

427 The first three columns of Table #3 further subdivide the fractional occurrence of low clouds
428 with CBH > 450 m into the fraction of time that the AAD depolarization lidar was fully or
429 heavily attenuated by the low-cloud layer, followed by the fraction of time it was lightly
430 attenuated, or the lidar data are missing or bad. (The sum of Table #3 columns 1-3 is equal to the
431 percentage of time that there are cloud layers with CTH < 3 km and CBH > 450 m listed in Table
432 #1, column 6). As discussed in section 2, we still retrieve a cloud base phase for lightly
433 attenuating cloud layers by defining the cloud layer extending from CBH-100 m through
434 CBH+300 m. Regarding bad data, in addition to the 17 days of bad data in August and
435 September (mentioned at the end of Section 2.2) we also filter out a small number of individual
436 data points with unphysical values that are significantly lower or higher than the range of
437 integrated backscatters reported in Mace et al. [2020], e.g. $\gamma < 0.02 \text{ sr}^{-1}$ and $\gamma > 0.2 \text{ sr}^{-1}$. These
438 individual points comprise about 1.2% of data in AM, 0.7% of data in JJA and only 0.2% of data
439 in SON. From August-October, the lidar performance (particularly the cross-polarization
440 channel) degraded and required more meticulous correction; see Supporting Information.

441

442 As discussed in section 2 (see also Fig. 1) the cloud base phase of warm-topped clouds are
443 overwhelmingly found to be liquid phase (95%), as one expects. For cold-topped clouds (CTT \leq
444 0°C), the highlighted section of Table #3 (columns 4-6) gives the *relative* occurrence frequency
445 of the cloud base phase such that liquid + HOI/mix + ROI/mix sum to 100% in each season. In

446 qualitative agreement with previous studies (e.g. MP2018), we also find that the majority of
 447 cold-topped clouds are liquid phase at cloud base (86% in the April-Nov. period), and this is true
 448 in all months/seasons for which we have measurements. There is, arguably, a slightly greater
 449 occurrence of frozen and mixed/uncertain cloud base phase in fall (AM) and winter (JJA)
 450 compared to spring (SON). Removing the lightly attenuating clouds does not significantly
 451 change these relative occurrences.

Season	CTH<3km, CBH>450m, fully or heavily attenuated [%]	CTH<3km, CBH>450m, lightly attenuated (retrieval uses cloud base+300m) [%]	CTH<3km, CBH>450m, AAD lidar data missing/bad [%]	Liquid phase cloud base (CTT≤0°C clouds) [%]	Frozen or mixed HOI cloud base (CTT≤0°C clouds) [%]	Frozen or mixed ROI cloud base (CTT≤0°C clouds) [%]
AM	31.8±3.4	5.3±0.7	1.2±0.7	83.3±1.9	7.1±1.5	9.6±1.4
JJA	27.6±2.5	5.4±0.7	6.0±1.9	85.2±1.8	10.1±1.6	4.7±0.9
SON	31.7±2.8	8.3±1.0	4.6±1.7	88.2±1.8	8.6±1.7	3.2±0.7
April- Nov.	30.1±1.6	6.4±0.5	4.4±1.0	85.7±1.1	8.8±0.9	5.5±0.6

452 *Table 3: Occurrence frequency (relative to all time) when low clouds are present with CBH>450 m and when depolarization*
 453 *lidar is (i) fully or heavily attenuated, (ii) not fully attenuated but still able to retrieve a cloud base phase, and (iii) missing or*
 454 *bad. The highlighted columns give the relative occurrence frequency of each cloud phase (these column sum to 100%) for times*
 455 *when CTT<0; for example, when cold-topped clouds are present and lidar data is good in April-May, 83.3% are liquid at cloud*
 456 *base, 7.1% HOI/mix and 9.6% ROI/mix, summing to 100%.*

457

458 3.3 Precipitation just below cloud base

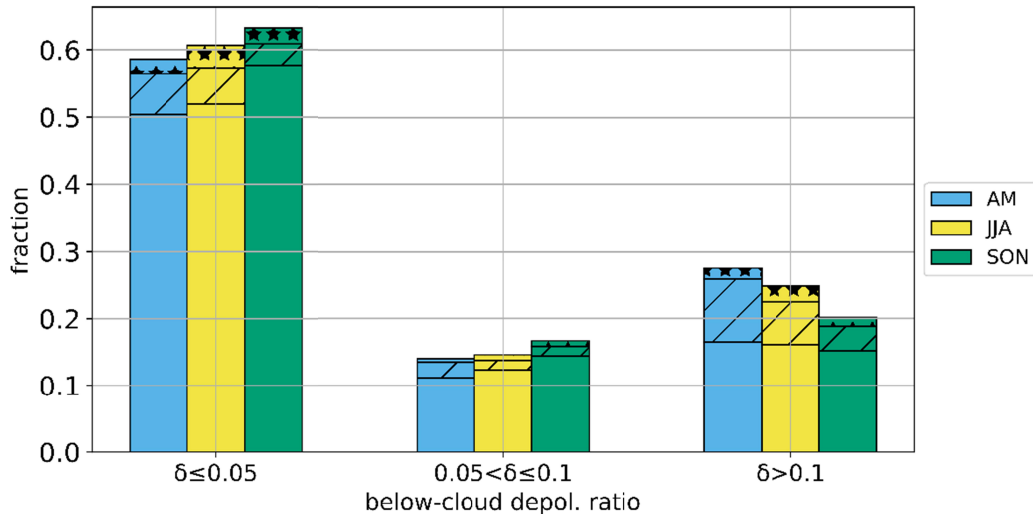
459

460 Table #4 contains seasonal occurrence frequencies of below-cloud precipitation, as well as the
 461 fraction of time that this precipitation reaches the surface (detected with the blended radar-
 462 disdrometer-tipping bucket dataset). The occurrence statistics in Table #4 are the relative
 463 percentages, meaning the fraction of good data when low clouds are present with CBH > 450 m
 464 and CTH < 3 km, and the condition listed in each column is met. For example, for the duration of
 465 the dataset (April-November) warm-topped low clouds only occur about 5% of the time (column
 466 7, Table #1); when present, 72% of the time these warm-topped clouds are precipitating 150 to
 467 250 m below the ceilometer cloud base. Overall, Table #4 shows that a significant majority (68%
 468 to 80%) of low clouds have precipitation falling from them, regardless of whether they are warm
 469 or cold-topped, and much of this precipitation does not reach the surface. The high occurrence of
 470 precipitation just below cloud base shown here – as well as the difference between below-cloud

471 precipitation and precipitation at (or near) the surface – is consistent with Silber et al. [2021],
 472 who examine the prevalence of precipitation from supercooled clouds in the Antarctic, Stanford
 473 et al. [2023] who report similar below-cloud precipitation occurrence using the MICRE radar,
 474 and nearby ship campaigns like MP18. Most of this precipitation is comprised of small particles
 475 and has a precipitation rate below 0.5 mm/hour most of the time [Wang et al. 2015, Tansey et al.
 476 2022].
 477

Season	Warm low cloud precipitation [%]		Cold low cloud precipitation [%]	
	below-cloud	at surface	below-cloud	at surface
AM	72.1±4.6	41.3±5.8	72.9±4.2	42.2±4.4
JJA	78.8±3.4	47.0±4.4	79.8±2.1	51.3±3.4
SON	64.2±3.6	34.4±3.9	68.1±2.9	40.9±3.4
April- Nov.	71.4±2.2	40.6±2.6	74.0±1.7	45.3±2.1

478 *Table 4: Percentage relative to the subset of low cloud with CTH < 3 km, CBH > 450 m that have precipitation detected (i) in the*
 479 *layer extending from CBH-250 m to CBH-150 m and (ii) at the surface (using the radar-disdrometer-tipping bucket blended data*
 480 *product).*



481 *Figure 3: Fraction of below-cloud precipitation for clouds with CTT < 0°C in each season by (i) cloud base phase (solid*
 482 *bars=liquid, dashes=mix/uncertain, stars=ice) and (ii) layer-averaged δ_L (horizontal axis).*
 483

484 In Fig. 3 we examine the relationship between cloud-base phase and below-cloud precipitation
 485 phase for cold-topped clouds. Precipitating clouds have been grouped by their below-cloud δ_L
 486 ranges, where $\delta_L < 0.5$ means likely liquid phase precipitation and $\delta_L > 0.1$ means likely ice phase
 487 precipitation (that is, snow, graupel or ice pellets), as discussed in section 2. The hatching on
 488 each bar indicates the cloud base phase: solid means liquid, stripes are mixed/ambiguous and
 489 stars mean a pure ice phase cloud base (ROI or HOI crystals). Fractions in each season are

490 relative to the number of successful phase retrievals; in other words, bars of each color (each
491 season) sum to 1. In good agreement with MP18, we find that a significant fraction of low
492 clouds are producing ice phase precipitation. MP18 find that 32% of precipitating low clouds
493 (they used $CTH < 4$ km) with below-freezing cloud base temperatures were ice phase or
494 producing ice phase precipitation (see their table #1). The data in our Fig. 3 is restricted to cold
495 cloud tops (rather than cloud bases), nonetheless we similarly find 37 to 41% of cold clouds are
496 producing ice or mixed/ambiguous phase precipitation (sum of last two columns), depending on
497 the season. Unlike MP18, however, we also find that frozen precipitation is often falling from
498 low clouds with liquid phase cloud bases. We will discuss this difference in more detail in
499 Section 4.

500

501 3.4 Below-cloud precipitation phase by radar dBZ

502

503 In this section we build upon results presented in MP18 regarding the relationship between δ_L
504 and radar reflectivity (dBZ) in below-cloud precipitation. Specifically, MP18 find that during the
505 CAPRICORN experiment a W-band reflectivity in excess of -10 dBZ has δ_L values that are
506 predominately larger than 0.05, indicative of ice-phase. This result has obvious practical value in
507 terms of interpreting CloudSat and other radar observations, but also suggests that much (if not
508 most) of the accumulated precipitation involves ice-phase microphysical processes (more on this
509 in Section 4).

510

511 In Fig. 4 we present 2D joint histograms of lidar depolarization ratio and radar reflectivity
512 associated with the below-cloud precipitation falling from cold-topped clouds ($CTT \leq 0^\circ\text{C}$) for
513 three seasons (AM, JJA, SON). The color indicates the number of counts (of 5-minute periods)
514 which fall into each histogram grid cell. We overlay lines at -10 dBZ and the three δ_L thresholds
515 indicative of liquid, mixed/ambiguous, and ice phase to separate the histograms into six zones.
516 The relative percentage of counts in each zone is also overlaid. Fig. 4 shows that for reflectivity
517 factors below -10 dBZ, the precipitation is predominately liquid phase, and the occurrence of
518 unambiguously ice phase precipitation ($\delta_L > 0.1$) greatly increases above the -10 dBZ line.
519 Nonetheless, liquid phase particles ($\delta_L < 0.05$) are not rare above -10 dBZ. We examine the
520 relative phase occurrence in more detail in Fig. 5.

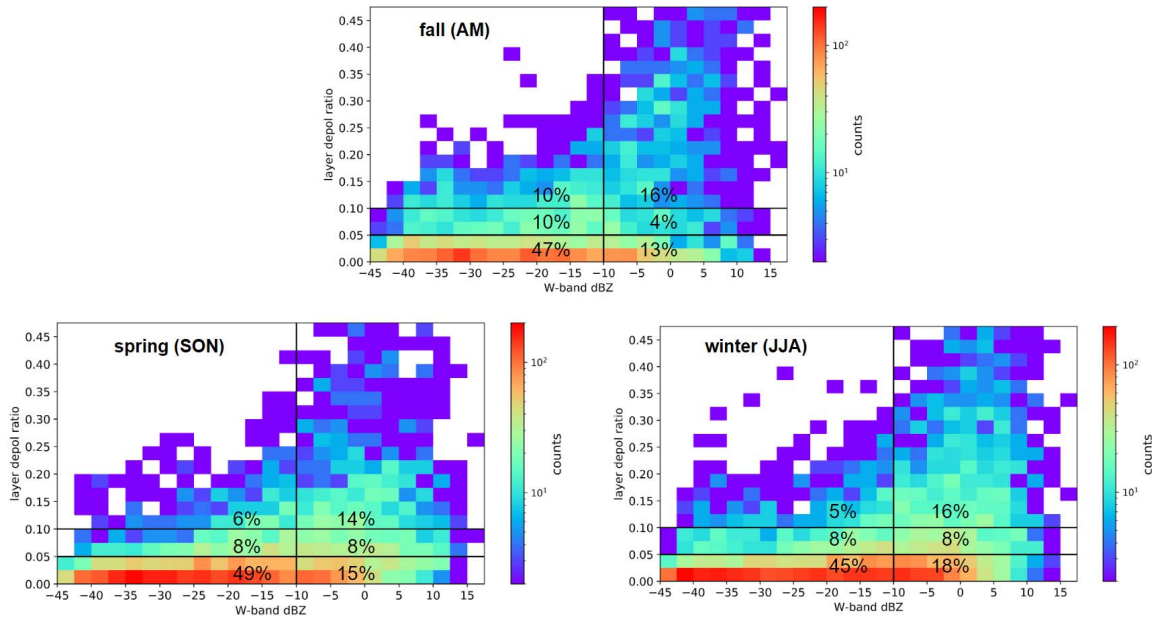


Figure 4: 2D histograms of δ_L vs. dBZ for precipitation below the bases of cold clouds, with the percentage of counts above/below -10 dBZ and in each δ_L phase regime.

521
522
523

524 In Fig. 5, we depict the relative occurrences of each phase category as a function of the
525 reflectivity binned in steps of 2 dBZ, grouped by season. Normalization is done for each season
526 such that for a particular season and reflectivity factor, the liquid, ambiguous and frozen
527 fractional occurrence points sum to one. As inferred from Fig. 4, there is a significant increase in
528 the relative occurrence of ice starting at about -10 dBZ. However, it is not until one reaches a
529 reflectivity near 0 dBZ that ice is unambiguously more frequent than liquid phase precipitation.

530

531 Overall, the result in Figs. 4 and 5 confirm the finding from MP18, though they suggest the
532 transition is more gradual. Possibly this difference is due to the short duration (a few weeks) of
533 the dataset used by Mace and Protat. Remarkably, there appears to very little seasonal variation
534 in this relationship. Taken at face value, the data in Fig. 5 suggest there is a greater tendency for
535 ice phase precipitation in April and May, but given that the data still amount to (less than) a year
536 of observations, this small difference may well not be significant.

537

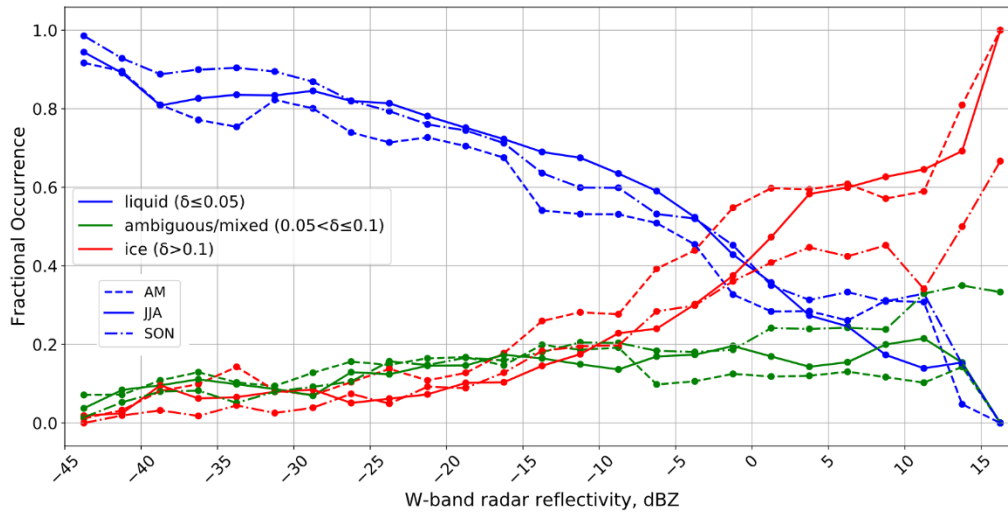


Figure 5: Fractional occurrence of liquid, ambiguous/mixed phase and ice at each reflectivity value. Phase-denominated points from a particular season sum to 1 in each reflectivity bin.

538
539
540

541

3.5 Below-cloud depolarization ratios and precipitation at the surface

542
543

544 In Fig. 6 we examine the relationship between the lidar below-cloud precipitation phase and the
 545 surface disdrometer (Parsivel2) derived particle type. Somewhat similar to Fig. 3, we plot the
 546 occurrence of surface precipitation in each below-cloud δ_L regimes (representing likely liquid,
 547 mixed/ambiguous, and likely ice) in each season. Here we include all clouds regardless of the
 548 CTT (though we hasten to add that most warm-topped clouds have a CBH too low for the below-
 549 cloud precipitation phase retrieval to be applied, and more than 80% of the clouds in this analysis
 550 have a CTT $< 0^\circ\text{C}$). Precipitation reaching the surface at Macquarie Island is most often
 551 comprised of particles that are too small (diameters less than about 1 mm) for their type to be
 552 accurately determined by the surface Parsivel disdrometer, and Tansey et al. [2022] simply
 553 categorize these hydrometeors as “small particle precipitation”. The top panel in Fig. 6 shows the
 554 lidar depolarization ratios in the range 250 to 150 m below cloud base for particles categorized as
 555 “small” at the surface, while the bottom panel in Fig. 6 shows the below-cloud depolarization
 556 ratios when there are large particles at the surface. In the lower panel, stars denote large particles
 557 that are ice (frozen) or mixed phase at the surface. $\sim 62\%$ of small surface particles have a
 558 below-cloud phase that is likely liquid and $\sim 22\%$ likely ice, with the remainder being ambiguous,
 559 with little seasonal variability. Most large particles, on the other hand, are likely ice phase just
 560 below cloud base, with seasonal differences being more pronounced. SON has a lower fraction

561 of below-cloud particles in the likely frozen category (58%) than AM & JJA (75% & 77%,
562 respectively); instead SON has a larger fraction of mixed/ambiguous (27%) than AM & JJA
563 (12% & 14%). In Tansey et al. [2022], our disdrometer analysis of precipitation at the surface
564 also shows that SON contains more (large droplet) rain than MAM & JJA. Large particle
565 precipitation includes essentially all surface precipitation with a precipitation rate above 0.5
566 mm/hr and is responsible for most of the total accumulated precipitation at Macquarie Island.
567 The solid portion of the bars in this lower panel shows the fraction of large particle precipitation
568 at the surface that is identified as rain. As the sizeable fraction of solid bar associated with
569 below-cloud $\delta_L > 0.1$ (ice) demonstrates, ice (frozen) phase precipitation often melts before it
570 reaches the surface and there is very little “warm rain” (rain that has formed without ice
571 processes being involved) at Macquarie Island that is not small particle precipitation (that is,
572 drizzle).

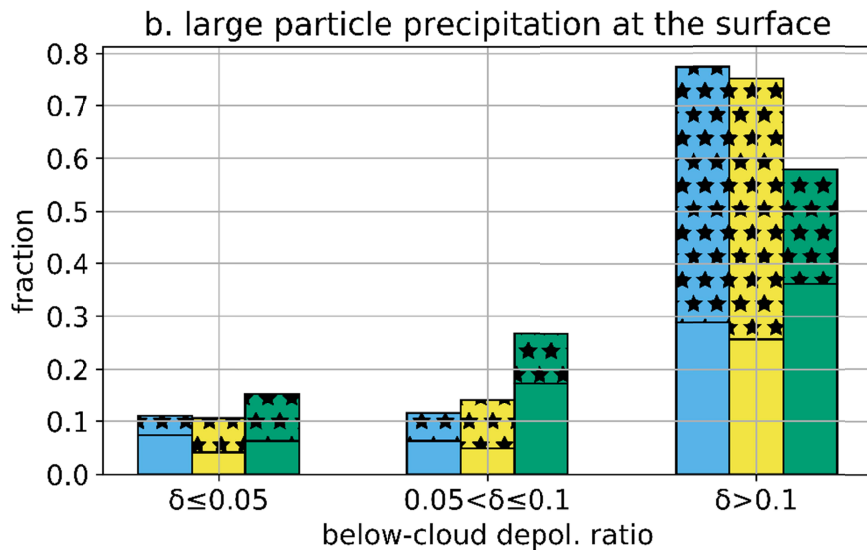
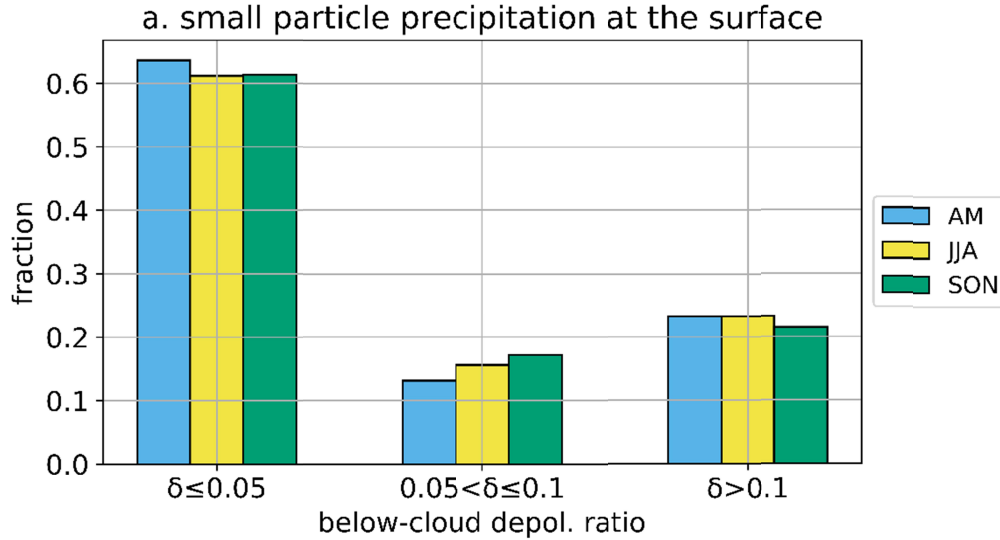


Figure 6: *a.* Small-particle precipitation at the surface by season, split into different lidar δ_L phase regimes in the layer CBH-200 m through CBH-100 m. *b.* Same as *a.*, but for large particles. Precipitation for both warm- and cold-topped clouds is included. Solid colors represent rain, stars represent mixed/frozen as designated by the surface disdrometer. Phase specification is only possible for large particles (diameters $> \sim 1$ mm) with the Parsivel disdrometer.

4. Discussion and Conclusions

Previous studies have examined the frequency of ice formation in SO low clouds from cloud top with satellite remote sensing, as well as from cloud base with radar and polarization lidar [Huang et al. 2015, Mace & Protat 2018, Mace et al. 2020, Mace et al. 2021a,b]. Satellites provide valuable insight into inter-annual and spatial variability of SO cloud properties, which the MICRE data cannot. Nonetheless, with the 7 consecutive months of depolarization lidar and almost 12 months of radar, ceilometer, surface disdrometer data collected during MICRE, we are

587 able to build on these previous studies. We summarize below the main results in their order of
588 presentation from sections 3.1 through 3.5, and discuss their implications.

589

590 **1)** During MICRE, low clouds occurred ~65% of the time (annually averaged), with DJF 2016-
591 2017 having slightly less low cloud cover than JJA 2016. About $\frac{2}{3}$ of low clouds are cold-
592 topped (CTT < 0°C). On average, cold-topped low clouds are geometrically thicker and have
593 cloud bases that are higher in altitude than warm-topped clouds, with only small seasonal
594 differences.

595

596 Shipborne lidar-radar combined observations (MARCUS: Jan.-March 2018; CAPRICORN I:
597 March-April 2016; CAPRICORN II: Jan.-Feb. 2018) in the vicinity of Macquarie Island
598 (spanning latitudes 43°S to 68°S) have provided similar results. We find relatively similar cloud
599 occurrence frequencies (Table #1) to those from the ship campaigns, even given the differences
600 in location and criteria used to define low clouds. Protat et al [2017] report an absolute
601 occurrence frequency of 77% for low clouds (1 week of data in March 2015) and MP18 report
602 low clouds occur 65% of the time (March-April 2016), which matches the frequency we find
603 during MICRE (ranging from 60-69% depending on the season). The seasonal differences across
604 the MICRE year are small in both cloud occurrence frequencies and boundaries (base/top heights
605 and geometric thicknesses; Table #2), although we find that CBH is higher on average in DJF &
606 SON for both warm and cold clouds. While much of the concern regarding SO low clouds has
607 focused on their shortwave impacts, as previously discussed by Hinkelman & Marchand [2020],
608 cloud base height is important to the downward longwave flux, and downward longwave surface
609 fluxes in the operational CERES SYN product are biased low in this region because satellite-
610 estimated cloud bases used by CERES are too high and cold, especially at night.

611

612 **2)** Cloud base phase retrievals show that cold-topped low clouds are overwhelmingly liquid
613 phase (~85%) in all seasons for which we have both depolarization lidar and radar
614 measurements (April-Nov. 2016). During MICRE, there was a slightly greater occurrence of
615 frozen and mixed/uncertain phase clouds in fall (AM) and winter (JJA) compared to spring
616 (SON), but the difference is small (only a few percent). Given the potential for interannual

617 variability, it would take several more years of data to establish whether or not this difference
618 represents a true seasonal cycle.

619
620 Retrievals based on both satellite imagers (such as MODIS) and spaceborne lidar (CALIPSO)
621 indicate the most SO cold-topped low clouds are predominantly liquid phase at cloud top [e.g.,
622 Huang et al. 2015]. Mace et al. [2021a] suggest that as little as 3% of the time, low clouds (CTH
623 < 3 km) have ice-phase cloud tops based on CALIPSO measurements (this number includes both
624 warm and cold topped clouds). We stress that having mostly liquid-phase cloud particles at either
625 cloud top or cloud base does not mean that there is no ice in the cloud, or that ice phase
626 processes are not active or important. As we discuss in more detail below, like MP18, we do find
627 ice phase precipitation frequently falling from these supercooled liquid clouds.

628
629 Mace et al. [2021a] describe CALIPSO's tendency to identify clouds as liquid phase, even when
630 ice is precipitating from them, as a failure or error of the satellite retrieval to identify the clouds
631 as mixed phase. We do not dispute that the presence of precipitating ice must mean there are
632 some small (cloud-droplet-sized) ice particles in the cloud. Nor do we dispute the Mace et al.
633 [2021a] conclusion that the phase is identified to be liquid because visible photon scattering
634 occurs predominantly in the upper portion of the cloud, whereas the ice is located deeper in the
635 cloud. But for this same reason, we suggest that CALIPSO and imager retrievals (based on the
636 scattering of visible photons) be referred to as "cloud top phase" retrievals, with no expectation
637 that the retrieval will indicate whether or not ice is present deeper in the cloud. This is not
638 entirely an issue of semantics. The identification of the cloud top phase as liquid (independent of
639 ice precipitating from the bottom) has value in that it tells us something about the angular
640 scattering dependence of the cloud, and how to convert measured shortwave radiances into
641 shortwave fluxes. It also tells us that we can reasonably estimate cloud optical depth, liquid
642 water path, and effective radius using visible-and-near-IR (MODIS-like [Nakajima & King
643 1990]) techniques that assume small spherical water droplets. In short, distinguishing cloud
644 phase from precipitation phase is valuable in the same way as splitting the hydrometeor particle
645 size distribution into separate cloud and precipitation components. An objective for retrievals
646 should be to identify both the cloud and precipitation phases.

647

648 Regarding the cloud base phase, our results differ from MP18; MP18 suggest that cloud base
649 phase is predominantly ice when ice-phase precipitation is falling from low clouds, and thus,
650 they find that cloud bases are glaciated a larger fraction of the time than we find here (~29% vs.
651 ~15% at most, since the 15% includes ambiguous cases). We speculate that this difference
652 reflects a weakness in the cloud base phase retrieval used by MP18. The cloud base phase
653 retrieval used in this article accounts for multiple scattering. This is not true of the approach used
654 by MP18, which assumes that multiple scattering can be neglected in the first bin above cloud
655 base. This is problematic because to the degree that the lidar backscatter is dominated by small
656 cloud droplets, one expects that multiple scattering will be present and will increase the
657 depolarization ratio; if scattering is not dominated by small cloud droplets, the contribution from
658 any glaciated precipitation might also appreciably increase the depolarization ratio. In some
659 larger sense, it is unlikely that clouds composed primarily of small frozen particles at cloud base
660 would be composed primarily of small liquid particles at cloud top. Therefore, ice-phase cloud
661 base occurrence should not substantially exceed ice-phase cloud top occurrence – and even our
662 finding that ~85% of cloud bases are liquid should be treated as a lower bound for the occurrence
663 of liquid phase clouds (i.e. clouds where most small cloud-size particles are liquid phase).

664

665 **3)** A significant majority of low clouds have precipitation falling from them regardless of CTT.
666 Much of this precipitation does not reach the surface (Table #4).

667

668 The high occurrence of precipitation just below cloud base shown in Table #4, as well as the
669 difference between below-cloud precipitation and precipitation at (or near) the surface, is
670 consistent with Silber et al. [2021] examining the prevalence of precipitation from Antarctic
671 supercooled clouds. It is also consistent with results presented by Stanford et al. [2023,
672 submitted] for Macquarie Island based on the same W-band radar and ceilometer data used here,
673 but processed independently. Stanford and co-authors provide a more in-depth analysis
674 examining the dependence of precipitation on the radar sensitivity and distance from the cloud
675 and surface. They also present a comparison of the observed data with GISS-ModelE3
676 simulations.

677

678 It is worth stressing that much of this light precipitation is too light for CloudSat to detect (in no
679 small part because of surface clutter) or to identify as precipitation (rather than cloud) because
680 the reflectivity is often < -15 dBZ, and the cloud base position is unknown, making it difficult to
681 distinguish precipitation from cloud [Tansey et al. 2022, Stanford et al. 2023]. While these very
682 light precipitation rates contribute only weakly to total accumulation at the surface, they have
683 important implications for aerosol-cloud interactions and boundary layer thermodynamics. In
684 particular, coalescence scavenging has been shown to be the primary sink of cloud condensation
685 nuclei and has a large effect on cloud droplet number concentration, even at very low
686 precipitation rates (e.g., 0.01 mm/hr) undetected by CloudSat [Kang et al. 2022]. This is true in
687 both liquid and mixed phase precipitating clouds over the SO.

688
689 On a minor note, recent studies by Mace et al. [2021a,b] and MP18 report somewhat lower
690 precipitation occurrence rates for SO low clouds based on W-band radar observations from the
691 MARCUS and CAPRICORN ship cruises. In these studies, precipitation is identified when
692 column or below-cloud maximum reflectivity is greater than -20 dBZ. In our study, we identify
693 precipitation based on the presence of hydrometeors more than 150 m below the lidar ceilometer
694 cloud base (regardless of reflectivity). We very often identify below-cloud precipitation with
695 reflectivity factors below -20 dBZ, and therefore it is not surprising that these different criteria
696 result in somewhat different occurrence statistics. We plan to explore this difference in future
697 research focused on an analysis of MICRE-retrieved cloud and precipitation microphysical
698 properties.

699
700 **4)** We observe that low clouds often produce ice phase precipitation, in agreement with MP18.

701
702 Similar to MP18, we find $\sim 40\%$ of cold-topped low clouds are producing ice or
703 mixed/ambiguous phase precipitation. Ice/mixed phase cloud (and precipitation) occurrence is
704 often episodic in nature. Lang et al. [2021] utilize a CAPRICORN case study to study ice/mixed
705 phase – which alternates within patches of supercooled liquid – in open mesoscale cellular
706 convective systems governed by shallow convection. They demonstrate a clear relationship
707 between shallow convection and intermittently precipitating mixed phase clouds. Our extended
708 time series from MICRE shows that 58% of mixed/frozen cloud bases persist for only a single 5-

709 minute period. A lower fraction of 40% persist 10 to 20 consecutive minutes; only 2% persist for
710 a period longer than 20 minutes. These statistics substantiate the notion that frozen/mixed phase
711 particles at cloud base generally exist within patches of supercooled liquid.

712

713 **5)** Also following MP18, we do find a significant increase in ice phase precipitation for below-
714 cloud reflectivity factors in excess of -10 dBZ, but only above ~ 0 dBZ does ice surpass liquid
715 as the predominant phase.

716

717 The relationship between reflectivity and phase is robust across the period examined (April -
718 November 2016), and appears to be true during the summer as gauged from SOCRATES aircraft
719 measurements [Kang et al. 2023, submitted]. Of course, part of the reason for this relationship is
720 that radar reflectivity is a strong function of particle size and ice phase precipitation tends to
721 form larger particles (see section 3.5), likely because of the Wegener–Bergeron–Findeisen
722 process and efficient growth by accretion. Nonetheless, this suggests large reflectivity factors
723 associated with cold-topped low clouds can be taken as indicative of ice-phase precipitation. If
724 broadly representative of the SO, as seems likely, this result is very useful for the interpretation
725 of satellite and aircraft radar data and the retrieval of precipitation rates.

726

727 **6)** Most drizzle (reflectivity < -10 dBZ, small-particle precipitation) is liquid phase directly
728 below cloud base, while most large-particle precipitation is found to be ice phase.

729

730 As documented in our earlier study [Tansey et al. 2022], total accumulated surface precipitation
731 is dominated by precipitation that contains large particles (particles with diameters $> \sim 1$ mm).
732 The large-particle precipitation is classified as rain, ice pellets, wet snow or (dry) snow, based on
733 the surface disdrometer retrieved particle size and velocity. Here we find that most of the large-
734 particle precipitation identified by the disdrometer has a phase that is ice or mixed/ambiguous
735 just below cloud base. This includes rain, meaning that most rain has formed from the melting
736 of ice. The prevalence of ice precipitation underscores the importance of understanding and
737 modeling both liquid and ice phase processes in SO low clouds. As Mülmenstädt et al. [2015]
738 argue, this has important consequences for climate change.

739

740 In summary, the MICRE campaign has produced the longest timeseries of surface radar,
741 ceilometer, and depolarization lidar observations to date over the SO. Uncertainty due to the lidar
742 performance and calibration is a consideration for MICRE, particularly in August-October,
743 during which time an abrupt step in the cross-polarization channel counts emerged. This was
744 corrected by scaling depolarization ratios by a calibration factor determined using stable, well-
745 calibrated periods earlier in the time series (see Supporting Information). Furthermore, the
746 present data enable a 7-month-long analysis of cloud and precipitation phase. The combination
747 of radar and depolarization lidar unfortunately does not extend to DJF, however, and
748 consequently, we cannot estimate the degree to which summer low clouds produce less ice-phase
749 precipitation. In an absolute sense, there will be less ice, simply because there is less cold-topped
750 cloud. We speculate whether there is also a difference in ice amount driven by availability of
751 aerosols that serve as primary INP (which appear to have a strong biological connection in data
752 collected during the SH summer [Twohy et al. 2021]). Differences in boundary layer
753 thermodynamics may also affect secondary ice processes. While the SOCRATES aircraft
754 observations have added substantially to existing in situ data for the SO, there remains a strong
755 need for more in situ data, especially measurements during the winter and data for use in process
756 modeling studies. This is not to discount the value of collecting additional surface data from
757 Macquarie Island. There does appear to be a modest level of variability (~5%-10%) from April
758 to November. But given the potential for interannual variability, it will take several more years
759 of data to be confident that this is the climatological norm. Additional data would also be very
760 useful in estimating cloud feedbacks, for example, following the approach in Terai et al. [2019]
761 applied to measurements at several Northern Hemisphere ARM sites.

762 Data availability

763 Data collected during MICRE are available via the ARM data archive (<https://adc.arm.gov/>). The
764 radar-lidar cloud base and below-cloud precipitation retrievals, as well as 5-minute reduced radar
765 and lidar time series, are available at [*submitted to the ARM archive, DOI's pending*].

766 Acknowledgments

767 This work was supported by the U.S. Department of Energy Atmospheric System Research
768 program through Grant DE-SC0016225 and NASA through Grant NNX16AM05G. Technical
769 and logistical support for the deployment to Macquarie Island were provided by the Australian

770 Antarctic Division through Australian Antarctic Science Project 4292, and we thank George
771 Brettingham-Moore, Ken Barrett, Nick Cartwright, Nick Cole (deceased), Emry Crocker, Terry
772 Egan, John French, Eric King (deceased), Ian McRobert, Lloyd Symons, Peter de Vries and
773 Steven Whiteside for all of their assistance. We would also like to thank Adrian McDonald for
774 providing the University of Canterbury ceilometer data used to supplement the ARM ceilometer.

775 References

- 776 • Bodas-Salcedo, A., P.G. Hill, K. Furtado, K.D. Williams, P.R. Field, J.C. Manners, P. Hyder,
777 Kato, S. (2016). Large Contribution of Supercooled Liquid Clouds to the Solar Radiation
778 Budget of the Southern Ocean. *J. Climate*, 29, 4213-4228, [https://doi.org/10.1175/JCLI-D-](https://doi.org/10.1175/JCLI-D-15-0564.1)
779 15-0564.1
- 780 • Ceppi, P., Y.-T. Hwang, D. M. W. Frierson, and D. L. Hartmann (2012). Southern
781 Hemisphere jet latitude biases in CMIP5 models linked to shortwave cloud forcing. *Geophys.*
782 *Res. Lett.*, 39, L19708, doi:10.1029/2012GL053115.
- 783 • Ceppi, P., Y.-T. Hwang, X. Liu, D. M. W. Frierson, and D. L. Hartmann (2013). The
784 Relationship Between the ITCZ and the Southern Hemispheric Eddy-Driven Jet, *J. Geophys.*
785 *Res. Atmos.*, 118, 5136–5146, doi:10.1002/jgrd.50461
- 786 • Ceppi, P., Hartmann, D., Webb, M. (2015). Mechanisms of the Negative Shortwave Cloud
787 Feedback in Middle to High Latitudes, *Journal of Climate*, 29, 139-157. DOI: 10.1175/JCLI-
788 D-15-0327.1
- 789 • Cesana, G. V., Khadir, T., Chepfer, H., & Chiriaco, M. (2022). Southern ocean solar
790 reflection biases in CMIP6 models linked to cloud phase and vertical structure
791 representations. *Geophysical Research Letters*, 49, e2022GL099777.
792 <https://doi.org/10.1029/2022GL099777>
- 793 • Delanoë, J., A. Protat, J.-P. Vinson, W. Brett, C. Caudoux, F. Bertrand, J. Parent du Chatelet,
794 R. Hallali, L. Barthes, M. Haeffelin, and Dupont, J.-C. (2016). BASTA, a 95 GHz FMCW
795 Doppler radar for cloud and fog studies. *J. Atmos. Oceanic Tech.*, 33, 1023-1038,
796 <https://doi.org/10.1029/95JD03068>
- 797 • DeMott, P. J., Hill, T. C. J., McCluskey, C. S., Prather, K. A., Collins, D. B., Sullivan, R. C.,
798 Ruppel, M. J., Mason, R. H., Irish, V. E., Lee, T., Hwang, C. Y., Rhee, T. S., Snider, J. R.,
799 McMeeking, G. R., Dhaniyala, S., Lewis, E. R., Wentzell, J. J. B., Abbatt, J., Lee, C.,
800 Sultana, C. M., Ault, A. P., Axson, J. L., Diaz Martinez, M., Venero, I., Santos-Figueroa, G.,
801 Stokes, M. D., Deane, G. B., Mayol-Bracero, O. L., Grassian, V. H., Bertram, T. H., Bertram,
802 A. K., Moffett, B. F., and Franc, G. D. (2016). Sea spray aerosol as a unique source of ice
803 nucleating particles, *P. Natl. Acad. Sci. USA*, 113, 5797–5803,
804 <https://doi.org/10.1073/pnas.1514034112>
- 805 • Fan, J., Ghan, S., Ovchinnikov, M., Liu, X., Rasch, P. J., and Korolev, A. (2011).
806 Representation of Arctic mixed-phase clouds and the Wegener-Bergeron-Findeisen process
807 in climate models: Perspectives from a cloud-resolving study, *J. Geophys. Res.*, 116,
808 D00T07, doi:10.1029/2010JD015375.
- 809 • Frey, W. & Kay, J. (2018). The influence of extratropical cloud phase and amount feedbacks
810 on climate sensitivity *Clim. Dyn.* 50:3097–3116 DOI 10.1007/s00382-017-3796-5

- 811 • Gettelman, A., Hannay, C., Bacmeister, J. T., Neale, R. B., Pendergrass, A. G., Danabasoglu,
812 G., et al. (2019). High climate sensitivity in the Community Earth System Model Version 2
813 (CESM2). *Geophysical Research Letters*, 46, 8329–8337. [https://doi.org/10.1029/
814 2019GL083978](https://doi.org/10.1029/2019GL083978)
- 815 • Hinkelman, L. M., Marchand, R. (2020). Evaluation of CERES and CloudSat surface
816 radiative fluxes over Macquarie Island, the Southern Ocean. *Earth and Space Science*, 7,
817 e2020EA001224. <https://doi.org/10.1029/2020EA001224>
- 818 • Hu, Y., Vaughn, M., McClain, C., Behrenfeld, M., Maring, H., Anderson, D., et al., (2007).
819 Global statistics of liquid water content and effective number concentration of water clouds
820 over ocean derived from combined CALIPSO and MODIS measurements. *Atmospheric
821 Chemistry and Physics*, 7(12), 3353–3359. <https://doi.org/10.5194/acp-7-3353-2007>
- 822 • Huang, Y., A. Protat, S. T. Siems, and M. J. Manton, 2015: A-Train observations of maritime
823 mid-latitude storm-track cloud systems: Comparing the Southern Ocean against the North
824 Atlantic. *J. Climate*, 28, 1920–1939, doi:10.1175/JCLI-D-14-00169.1.
- 825 • Huang Y, Siems ST, Manton MJ, Rosenfeld D, Marchand R, McFarquhar GM, Protat A.
826 (2016), What is the role of sea surface temperature in modulating cloud and precipitation
827 properties over the Southern Ocean? *J. Clim.* 29: 7453–7476. <https://doi.org/10.1175/JCLI-D-15-0768.1>.
- 829 • Huang, Y., Franklin, C.N., Siems, S.T., Manton, M.J., Chubb, T., Lock, A., Alexander, S.,
830 Klekociuk, A. (2015). Evaluation of boundary-layer cloud forecasts over the Southern Ocean
831 in a limited-area numerical weather prediction system using in situ, space-borne and ground-
832 based observations. *Q. J. R. Meteorol. Soc.*, 141, 2259–2276. DOI:10.1002/qj.2519
- 833 • Hwang, Y. & Frierson, D. (2013). Link between the double-Intertropical Convergence Zone
834 problem and cloud bias over Southern Ocean. *Proceedings of the National Academy of
835 Sciences of the United States of America*. 110, doi:10.1073/pnas.1213302110.
- 836 • Kang, L., Marchand, R. T., Wood, R., & McCoy, I. L. (2022). Coalescence scavenging
837 drives droplet number concentration in Southern Ocean low clouds. *Geophysical Research
838 Letters*, 49, e2022GL097819. <https://doi.org/10.1029/2022GL097819>
- 839 • Kay, J.E., C. Wall, V. Yettella, B. Medeiros, C. Hannay, P. Caldwell, C. Bitz. (2016). Global
840 Climate Impacts of Fixing the Southern Ocean Shortwave Radiation Bias in the Community
841 Earth System Model (CESM). *J. Climate*, 29, 4617-4636, [https://doi.org/10.1175/JCLI-D-15-
842 0358.1](https://doi.org/10.1175/JCLI-D-15-0358.1)
- 843 • Kollias, P., and Albrecht, B. (2005). Why the melting layer radar reflectivity is not bright at
844 94 GHz, *Geophys. Res. Lett.*, 32, L24818, doi:10.1029/2005GL024074.
- 845 • Kuma, P., McDonald, A. J., Morgenstern, O., Alexander, S. P., Cassano, J. J., Garrett, S.,
846 Halla, J., Hartery, S., Harvey, M. J., Parsons, S., Plank, G., Varma, V., and Williams, J.
847 (2020). Evaluation of Southern Ocean cloud in the HadGEM3 general circulation model and
848 MERRA-2 reanalysis using ship-based observations, *Atmos. Chem. Phys.*, 20, 6607–6630,
849 <https://doi.org/10.5194/acp-20-6607-2020>
- 850 • Lang, F., Huang, Y., Protat, A., Truong, S. C. H., Siems, S. T., & Manton, M. J. (2021).
851 Shallow convection and precipitation over the Southern Ocean: A case study during the
852 CAPRICORN 2016 field campaign. *Journal of Geophysical Research: Atmospheres*, 126,
853 e2020JD034088. <https://doi.org/10.1029/2020JD034088>
- 854 • Lauer, A., Bock, L., Hassler, B., Schröder, M., & Stengel, M. (2023). Cloud Climatologies
855 from Global Climate Models—A Comparison of CMIP5 and CMIP6 Models with Satellite
856 Data, *Journal of Climate*, 36(2), 281-311, DOI: 10.1175/JCLI-D-22-0181.1

- 857 • Löffler-Mang, M., J. Joss (2000). An Optical Disdrometer for Measuring Size and Velocity
858 of Hydrometeors. *J. Atmos. Oceanic Technol.*, 17(2), 130-139, <https://doi.org/10.1175/1520->
859 0426(2000)017<0130:AODFMS>2.0.CO;2
- 860 • Mace, G. G. (2010). Cloud properties and radiative forcing over the maritime storm tracks of
861 the Southern Ocean and North Atlantic derived from A-Train, *J. Geophys. Res.*, 115,
862 D10201, doi:10.1029/2009JD012517.
- 863 • Mace, G.G., and A. Protat. (2018) Clouds over the Southern Ocean as observed from the R/V
864 Investigator during CAPRICORN: Part I: Cloud occurrence and phase partitioning, *J. Appl.*
865 *Meteor. Clim.*, 57, 1783-1804. doi:10.1175/JAMC-D-17-0194.1.
- 866 • Mace, G. G., Benson, S., & Hu, Y. (2020). On the frequency of occurrence of the ice phase
867 in supercooled Southern Ocean low clouds derived from CALIPSO and CloudSat.
868 *Geophysical Research Letters*, 47, e2020GL087554. <https://doi.org/10.1029/2020GL087554>
- 869 • Mace, G. G., Protat, A., & Benson, S. (2021a). Mixed-phase clouds over the Southern Ocean
870 as observed from satellite and surface based lidar and radar. *Journal of Geophysical*
871 *Research: Atmospheres*, 126, e2021JD034569. <https://doi.org/10.1029/2021JD034569>
- 872 • Mace, G. G., Protat, A., Humphries, R. S., Alexander, S. P., McRobert, I. M., Ward, J., et al.
873 (2021b). Southern Ocean cloud properties derived from CAPRICORN and MARCUS data.
874 *Journal of Geophysical Research: Atmospheres*, 126, e2020JD033368.
875 <https://doi.org/10.1029/2020JD033368>
- 876 • Mallet, M. D., Humphries, R.S., Fiddes, S. L., Alexander, S. P., Altieri, K., Angot, H.,
877 Anilkumar, N., Bartels-Rausch, T., Creamean, J., Dall'Osto, M., Dommergue, A., Frey, M.,
878 Henning, S., Lannuzel, D., Lapere, R., Mace, G. G., Mahajan, A. S., McFarquhar, G. M.,
879 Meiners, K. M., Peeken, I., Protat, A., Schmale, J., Steiner, N., Sellegri, K., Thomas, J. L.,
880 Willis, M. D., Winton, V. H. L., Woodhouse, M. T., Miljevic, B., Simo, R., (2023).
881 Untangling the influence of Antarctic and Southern Ocean life on clouds. *Elementa Science*
882 *of the Anthropocene*, 11, 1, doi:10.1525/elementa.2022.00130
- 883 • McCluskey, C. S., Hill, T. C. J., Humphries, R. S., Rauker, A. M., Moreau, S., Stratton, P.
884 G., et al. (2018). Observations of ice nucleating particles over Southern Ocean waters.
885 *Geophysical Research Letters*, 45(11), 989–997. <https://doi.org/10.1029/2018GL079981>
- 886 • McCoy, I. L., McCoy, D. T., Wood, R., Regayre, L., Watson-Parris, D., Grosvenor, D. P.,
887 Mulcahy, J. P., Hu, Y., Bender, F. A.- M., Field, P. R., Carslaw, K. S., and Gordon, H.
888 (2020). The Hemispheric Contrast in Cloud Microphysical Properties Constrains Aerosol
889 Forcing, *P. Natl. Acad. Sci. USA*, 117, 18998–19006,
890 <https://doi.org/10.1073/pnas.1922502117>
- 891 • McFarquhar, G. M., Bretherton, C. S., Marchand, R., Protat, A., DeMott, P. J., Alexander, S.
892 P., Roberts, G. C., Twohy, C. H., Toohey, D., Siems, S., Huang, Y., Wood, R., Rauber, R.
893 M., Lasher-Trapp, S., Jensen, J., Stith, J. L., Mace, J., Um, J., Järvinen, E., Schnaiter, M.,
894 Gettelman, A., Sanchez, K. J., McCluskey, C. S., Russell, L. M., McCoy, I. L., Atlas, R. L.,
895 Bardeen, C. G., Moore, K. A., Hill, T. C. J., Humphries, R. S., Keywood, M. D., Ristovski,
896 Z., Cravigan, L., Schofield, R., Fairall, C., Mallet, M. D., Kreidenweis, S. M., Rainwater, B.,
897 D'Alessandro, J., Wang, Y., Wu, W., Saliba, G., Levin, E. J. T., Ding, S., Lang, F., Truong,
898 S. C. H., Wolff, C., Haggerty, J., Harvey, M. J., Klekociuk, A. R., & McDonald, A. (2021).
899 Observations of Clouds, Aerosols, Precipitation, and Surface Radiation over the Southern
900 Ocean: An Overview of CAPRICORN, MARCUS, MICRE, and SOCRATES, *Bulletin of the*
901 *American Meteorological Society*, 102(4), E894-E928. Retrieved Dec 5, 2022, from
902 <https://journals.ametsoc.org/view/journals/bams/102/4/BAMS-D-20-0132.1.xml>

- 903 • Mülmenstädt, J., O. Sourdeval, J. Delanoë, and J. Quaas (2015). Frequency of occurrence of
904 rain from liquid-, mixed-, and ice-phase clouds derived from A-Train satellite retrievals,
905 *Geophys. Res. Lett.*, 42, 6502–6509, doi:10.1002/2015GL064604.
- 906 • Nakajima, T., & King, M. D., (1990). Determination of the Optical Thickness and Effective
907 Particle Radius of Clouds from Reflected Solar Radiation Measurements. Part I: Theory. *J.*
908 *Atmos. Sci.*, 47, 1878–1893, [https://doi.org/10.1175/1520-](https://doi.org/10.1175/1520-0469(1990)047<1878:DOTOTA>2.0.CO;2)
909 [0469\(1990\)047<1878:DOTOTA>2.0.CO;2](https://doi.org/10.1175/1520-0469(1990)047<1878:DOTOTA>2.0.CO;2)
- 910 • O'Connor, E. J., Illingworth, A. J., & Hogan, R. J., (2004). A technique for autocalibration of
911 cloud lidar. *Journal of Atmospheric and Oceanic Technology*, 21(5), 777–786.
912 [https://doi.org/10.1175/1520-0426\(2004\)021%3C0777:ATFAOC%3E2.0.CO;2](https://doi.org/10.1175/1520-0426(2004)021%3C0777:ATFAOC%3E2.0.CO;2)
- 913 • Protat, A., Schulz, E., Rikus, L., Sun, Z., Y. Xiao, Y. and Keywood, M. (2017) Shipborne
914 observations of the radiative effect of Southern Ocean clouds, *J. Geophys. Res. Atmos.*, 122,
915 318–328, doi:10.1002/2016JD026061.
- 916 • Sallée, J.-B., Shuckburgh, E., Bruneau, N., Meijers, A. J. S., Bracegirdle, T. J., Wang, Z.,
917 and Roy, T. (2013). Assessment of Southern Ocean water mass circulation and
918 characteristics in CMIP5, models: Historical bias and forcing response, *J. Geophys. Res.*
919 *Oceans*, 118, 1830– 1844 doi:10.1002/jgrc.20135.
- 920 • Schuddeboom, A. J., & McDonald, A. J. (2021). The Southern Ocean radiative bias, cloud
921 compensating errors, and equilibrium climate sensitivity in CMIP6 models. *Journal of*
922 *Geophysical Research: Atmospheres*, 126, e2021JD035310.
923 <https://doi.org/10.1029/2021JD035310>
- 924 • Schneider, D. P., & Reusch, D. B. (2016). Antarctic and Southern Ocean Surface
925 Temperatures in CMIP5 Models in the Context of the Surface Energy Budget, *Journal of*
926 *Climate*, 29(5), 1689-1716. <https://doi.org/10.1175/JCLI-D-15-0429.1>
- 927 • Silber, I., Fridlind, A. M., Verlinde, J., Ackerman, A. S., Cesana, G. V., and Knopf, D. A.
928 (2021). The prevalence of precipitation from polar supercooled clouds, *Atmos. Chem. Phys.*,
929 21, 3949–3971, <https://doi.org/10.5194/acp-21-3949-2021>
- 930 • Tansey, E., Marchand, R., Protat, A., Alexander, S. P., & Ding, S. (2022). Southern Ocean
931 precipitation characteristics observed from CloudSat and ground instrumentation during the
932 Macquarie Island Cloud & Radiation Experiment (MICRE): April 2016 to March 2017.
933 *Journal of Geophysical Research: Atmospheres*, 127(5).
934 <https://doi.org/10.1029/2021JD035370>
- 935 • Terai, C. R., Zhang, Y., Klein, S. A., Zelinka, M. D., Chiu, J. C., & Min, Q. (2019).
936 Mechanisms behind the extratropical stratiform low-cloud optical depth response to
937 temperature in ARM site observations. *Journal of Geophysical Research: Atmospheres*, 124,
938 2127–2147. <https://doi.org/10.1029/2018JD029359>
- 939 • Tokay, A., Petersen, W. A., Gatlin, P., and Wingo, M. (2013), Comparison of Raindrop Size
940 Distribution Measurements by Collocated Disdrometers, *Journal of Atmospheric and*
941 *Oceanic Technology*, 30(8), 1672-1690, <https://doi.org/10.1175/JTECH-D-12-00163.1>
- 942 • Twohy, C. H., DeMott, P. J., Russell, L. M., Toohey, D. W., Rainwater, B., Geiss, R., et al.
943 (2021). Cloud-nucleating particles over the Southern Ocean in a changing climate. *Earth's*
944 *Future*, 9, e2020EF001673. <https://doi.org/10.1029/2020EF001673>
- 945 • Trenberth, K. and J. Fasullo. (2010), Simulation of present-day and twenty-first century
946 energy budgets over the Southern Ocean, *J. Climate*, 23, 440-454, doi:
947 0.1175/2009JCLI3152.1

- 948 • Wang, Z., S. Siems, D. Belusic, M. Manton, and Y. Huang. (2015), A climatology of the
949 precipitation over the Southern Ocean as observed at Macquarie Island. *J. Appl. Meteorol.*
950 *Climatol.*, 54, 2321-2337, doi:10.1002/grl.50986
- 951 • Williams, K.D., Webb, M.J. (2009), A quantitative performance assessment of cloud regimes
952 in climate models. *Clim Dyn* (2009) 33:141–157, doi: 10.1007/s00382-008-0443-1
- 953 • Wood, R. (2012), Stratocumulus Clouds, *Monthly Weather Review*, 140(8), 2373-2423., doi:
954 10.1175/MWR-D-11-00121.1
- 955 • Zelinka, M. D., Myers, T. A., McCoy, D. T., Po-Chedley, S., Caldwell, P. M., Ceppi, P., et
956 al. (2020), Causes of higher climate sensitivity inCMIP6 models. *Geophysical Research*
957 *Letters*, 47, e2019GL085782. <https://doi.org/10.1029/2019GL085782>

958 Supporting Information References

- 959 • Hu, Y., Liu, Z., Winker, D., Vaughan, M., Noel, V., Bissonnette, L., Roy, G., and McGill, M.
960 (2006) Simple relation between lidar multiple scattering and depolarization for water clouds,
961 *Opt. Lett.* 31, 1809-1811
- 962